PCCP

Accepted Manuscript

ROYAL SOCIETY OF CHEMISTRY

www.rsc.org/pccp

Journal Name

ARTICLE

Far- and near-field properties of gold nanoshells studied by photoacoustic and surface-enhanced Raman spectroscopies

V. Weber[a], A. Feis[b], C. Gellini[b], R. Pilot[a], P. R. Salvi[b], R. Signorini[a]

Gold nanoshells, with silica core and different core and shell dimensions, have been extensively investigated. Optical far-field properties, namely extinction and absorption, have been separately determined by means of spectrophotometry and photoacoustic spectroscopy, respectively, in the 440-900 nm range. The enhancement factor for surface-enhanced Raman scattering, which is related to near-field effects, has been measured from 568 to 920 nm. The absorption contribution to extinction decreases as the overall diameter increases. Moreover, absorption and scattering display different spectral distributions, the latter being red shifted. The Surface Enhanced Raman Scattering enhancement profile, measured using thiobenzoic acid as a Raman probe, is further shifted to the red. The latter result suggests that the enhancement is dominated by the presence of hot spots, which are possibly related to the surface roughness of gold nanoshell particles.

1. Introduction

Gold nanoshells (Au NSs), based on a silica core and a gold shell, are studied in a number of research fields, ranging from imaging[1] and photothermal therapy[2] to sensing,[3] thanks to their excellent optical properties and versatility. Different features of the nanoshell structure can be optimized in order to make them best suited for different applications:[4–7] for example, imaging requires strongly scattering nanoparticles,[1] on the other hand photothermal therapy calls for strongly absorbing systems.[2] Sensing exploits the ability of metal nanoparticles to localize the external applied electromagnetic field in tiny spatial regions, close to their surface, to enhance the analyte detection sensitivity.[8–10]

All these features are related to the far- and near-field properties of nanoparticles.[11] Light extinction, deriving from scattering and absorption, is often referred to as a far-field property, whereas the electromagnetic field localized at the surface is a typical near-field feature of the metal nanostructure.[12] Both properties are strongly related to the localized surface plasmon resonance (LSPR), i.e. the collective electron oscillation on the surface of the metal nanostructure, induced by an electromagnetic radiation with appropriate wavelength.[11]

The extinction spectrum of Au NSs is not only dependent on the total particle radius, but also on the inner dielectric core dimension.[13] It can be tuned from the visible to the near- and mid-IR by changing their size and geometry, in particular the core-to-shell dimension ratio.[14,15] Since the first studies on optical properties of Au NSs, interest has been focused on extracting the absorption and scattering contributions from the total extinction spectrum.[16,17] The issue has been extensively investigated by theoretical approaches. For instance, absorption and scattering profiles of nanoshell structures have been evaluated through Mie calculations.[5,17,18] Also, the Discrete Dipole Approximation (DDA) method has been used for Au NSs with a variety of core and shell dimensions, resulting in the indication that the extinction coefficient depends linearly on the total size but is independent of the core/shell ratio.[7,18,19] Increasing the former or decreasing the latter, the scattering contribution to the extinction rapidly increases.[18] Experimental approaches to the determination of the absorption and scattering contribution have been reported in literature only for other metal nanostructures, like metal spheres and rods.[20–22] To our knowledge, no experimental data are found for Au NSs.

The LSPR is also responsible for the generation of the electromagnetic near-field distribution around the plasmonic nanostructure surface.[8] The local field intensity is strongly

amplified close to the nanostructure and steeply decays moving away from the surface.[19,23] Taking advantage of this enhancement, surface-enhanced Raman spectroscopy (SERS) is able to detect analyte molecules in traces[9,24] even at a single-molecule level.[25] In addition, the measurement of the SERS enhancement at several wavelengths (using an appropriate Raman probe)[26,27] allows one to reconstruct the near-field dispersion of the metallic substrate: however such measurements, carried out with a high number of points, are not very common in literature[28,29] due to the very specialized equipment required to tune the excitation wavelength.

In our approach, far- and near-field properties of Au NSs, properly synthesized in solution, are studied by a combination of UV-Vis spectrophotometry, photoacoustic spectroscopy (PAS) and SERS. PAS, being insensitive to light scattering, is a technique which can isolate the absorption contribution to the extinction spectrum. Laser-induced PAS has been measured in an extended wavelength range within the LSPR band, following a method recently applied to simple gold nanoparticles.[30] Near-field properties have been determined by measuring the SERS enhancement factor at a very high number of excitation wavelengths.

2. Experimental

2.1 Reagents

Gold (III) chloride solution 30% w/w in dilute HCl, tetraethyl orthosilicate, (3-aminopropyl)trimethoxysilane (APTMS), formaldehyde solution, potassium carbonate, polyvinylpyrrolidone (PVP, average mol wt 40000) and thiobenzoic acid (TBA) were purchased from Sigma-Aldrich and used without further purification. Syntheses were performed in deionized Milli-Q filtered water.

2.2 Gold nanoshell preparation

The syntheses of gold nanoshells were performed following a literature procedure.[31] Two different silica cores, of 38 and 46 nm radius, were synthesized following Stöber method[32] and subsequently functionalized with APTMS. Gold nanoparticles of about 2 nm diameter, prepared through the synthesis described by Duff et al.,[33] were then added to the SiO_2@APTMS solution, to homogeneously decorate the cores. The growth of the gold shell is accomplished by a reduction, with formaldehyde, of a gold precursor aqueous solution added to the decorated silica particles. Four different Au NSs solutions were obtained, with core (R1) and total radius (R2) dimensions reported in Table 1 (named Au NS I-IV). The Au NSs concentrations were $2.8 \cdot 10^{10}$, $1.4 \cdot 10^{10}$, $2.3 \cdot 10^{10}$ and $0.5 \cdot 10^{10}$ Au NSs particles/ml for Au NS I, II, III and IV respectively.

To perform photoacoustic and SERS spectroscopy, the Au NSs solutions were sterically stabilized with PVP. In case of photoacoustic measurements, Au NSs solutions were diluted to an absorbance in the range 0.2 - 0.4 (for 1 cm optical path), at the laser excitation wavelength. For SERS spectroscopy, 10 µl of a $2 \cdot 10^{-4}$ M TBA solution were added to 990 µl of Au NSs solution, previously diluted to absorbance 1 (for 1 cm optical path) at the wavelength of the LSPR maximum. 150 µl of ethanol were added to the Au NSs samples in order to introduce an internal standard for self absorption monitoring. The final TBA concentration was therefore 1.7×10^{-6} M. This value is smaller than the amount required to provide full NSs surface coverage, insuring that no free TBA was present in solution.

The extinction spectra at this concentration did not change appreciably upon TBA addition.

2.3 Instrument and methods

2.3.1 Optical and morphological characterization

Extinction spectra of Au NSs samples were measured with a Cary5 Varian spectrophotometer, working in the 200-1200 nm region, using quartz cuvettes of 1 or 10 mm optical path. The colloidal samples were morphologically characterized through dynamic light scattering (DLS) and transmission electron microscopy (TEM). DLS is performed with a Malvern Zetasizer Nano ZS instrument, with 633 nm laser excitation. From the maximum of the DLS intensity peak and its standard deviation, the NSs dimension and the associated errors are extracted. TEM is performed using a Field-Emission Gun Tecnai G2 microscope operating at 100 kV. The dimensions, extracted from TEM analysis, are calculated by a statistical measurement of the diameter from different images. The associated error is calculated as the measurement standard deviation.

2.3.2 Photoacoustic spectroscopy

Photoacoustic signals were detected with a 1 MHz bandpass Panametrics V103-RM piezoelectric transducer clamped to the sample cuvette. Signals were amplified with a Panametrics 5660 B amplifier and averaged with a Tektronix TDS-3054B digitizing oscilloscope. The minimum number of signals was 512 for each average. The excitation source was a GWU – Lasertechnik GmbH optical parametric oscillator pumped by the third harmonic of a Quanta System Nd:Yag laser. Measurements in the near-IR region were performed with a Quanta System Nd:Yag laser-pumped dye laser. The pulse duration was ~10 ns and the repetition rate 10 Hz. The excitation wavelength was measured with a Mut Tristan fiber optic spectrophotometer. The incident laser energy was measured in front of the sample cuvette by a pyroelectric head energy meter before each measurement and it lies in the range 2-20 µJ. The incident laser beam was shaped by a rectangular slit with 1x10 mm size without focusing in the sample. The sample signals were compared to those of calorimetric references, consisting of $KMnO_4$ or $CuSO_4$ aqueous solutions. At most excitation wavelengths, the photoacoustic signals of reference and sample were recorded three times at increasing laser pulse energies. In some cases, signals at single laser energy were recorded. Corrections were applied to take into account small extinction differences between sample and reference.

2.3.3 Surface-enhanced Raman spectroscopy

Enhancement factor (EF) measurements were performed with two home-made Raman setups: a micro- and a macro-Raman. The macro-Raman setup is equipped with two different lasers. The CW Ti:Sapphire Laser, optically pumped by a CW Semiconductor Laser (Coherent, Verdi G7), is tunable in the 675-1000 nm range (Spectra Physics, 3900S). The Ar+/Kr+ gas laser (Coherent, Innova 70) provides the lines at 568 and 647.1 nm. Laser beams are filtered through a tunable laser plasma line filter (Laserspec III, Spectrolab) and focused on the sample by a cylindrical lens. The Raman scattering diffused by the sample is collected by a camera objective (CANON 50 mm f/1.2) and

coupled into the slit of a three stage subtractive spectrograph (JobinYvon S3000) by means of a set of achromatic lenses. The spectrograph is made up by a double monochromator (JobinYvon, DHR 320), working as a tunable filter rejecting elastic scattering, and a spectrograph (JobinYvon, HR 640). The Raman signal is detected by a liquid nitrogen cooled CCD (JobinYvon, Symphony 1024x256 pixels front illuminated). A polarization scrambler is mounted right in front of the spectrograph slit. The system is configured in a backscattering geometry by placing a tiny mirror in front of the collection objective to steer the beam from the cylindrical lens to the sample. The sample is mounted on a translation stage that allows moving it parallel and perpendicular with respect to the laser propagation direction.

The micro-Raman setup is equipped with a He–Ne laser, working at 633 nm (MellesGriot with output power of 35 mW) and a 785 nm diode laser (Xtra with output power of 500 mW). The laser beam was coupled to a microscope (Olympus BX 40) and focused on the sample by a 20x objective (Olympus SLMPL). The backscattered Raman signal was separated from the Rayleigh scattering by edge or notch filters and analysed with a 320 mm focal length imaging spectrograph (TRIAX-320 ISA) and a liquid nitrogen cooled CCD camera (Spectrum One, JobinYvon).

Measurements were performed in liquid solution in a 2 ml vial with optical path of 0.8 cm. Acquisition times were 20 and 30 seconds (with 10 spectra accumulation), for macro- and micro-Raman measurements, respectively.

2.3.4 Enhancement factor measurements

 EF profiles were performed in the range from 568 to 940 nm using the macro-Raman setup. In case of Au NS II sample, also micro-Raman measurements at 633 and 785 nm were performed, in order to compare the results of two different Raman setups. The Au NSs solution SERS efficiency was estimated by comparing the integrated Raman peak intensity of the 1000 cm^{-1} ring breathing mode (S_{12})[34] of TBA adsorbed on Au NSs with the intensity of the same band in pure liquid TBA. The two signals are normalized by the corresponding concentration of molecules. In order to account for the absorption of the incident laser and the scattered Raman light, propagating through the sample, ethanol was used as an internal standard; in particular we referred to its 875 cm^{-1} C-C stretching mode. Finally, the EF was worked out by means of the following relation:[35]

$$EF = \frac{I_{SERS}/c_{SERS}}{I_R/c_R} \cdot \frac{I_{sar}^R}{I_{sar}^{SERS}}$$

I_{SERS} and I_R are the integrated peak intensities of the S_{12} mode of TBA in the SERS and reference sample, respectively. c_R is the concentration of the reference sample and c_{SERS} is the concentration of the molecule in the NS sample. I_{sar}^R is the signal intensity of the ethanol reference band in an aqueous solution, having the same ethanol concentration as the SERS samples; I_{sar}^{SERS} is the intensity of the ethanol signal in the NS solution. The error on the EF values is determined by calculating, with 5 different integration methods, the integral of the TBA signal at 568 nm, where the signal is less intense and therefore most affected by mathematical error in the integral determination. The maximum relative error, calculated at 568 nm and applied for all the excitation wavelengths, turned out to be about 15% for all the samples.

3. Results

3.1 Optical and morphological characterization

The values of the inner radius, the total radius and of the R1/R2 ratio of Au NSs samples, obtained through DLS and TEM measurement, are reported in Table 1.

Table 1. Au NSs dimensions: inner (R1) and final radii (R2) and their ratio (R1/R2), measured by DLS and TEM.

Sample name	TEM			DLS		
	R1[nm]	R2[nm]	R1/R2	R1[nm]	R2[nm]	R1/R2
Au NS I(38-59)	38 ± 9	59 ± 15	0.64 ± 0.22	47 ± 14	60 ± 33	0.78 ± 0.49
Au NS II(38-63)	38 ± 9	63 ± 7	0.60 ± 0.16	47 ± 14	84 ± 34	0.56 ± 0.28
Au NS III(46-63)	46 ± 3	63 ± 3	0.73 ± 0.06	54 ± 15	66 ± 20	0.81 ± 0.14
Au NS IV(46-68)	46 ± 3	68 ± 4	0.68 ± 0.06	54 ± 15	98 ± 33	0.60 ± 0.24

As expected, TEM measurements give a smaller diameter with respect to the DLS analysis, which provides the hydrodynamic diameter and therefore an overestimation of the real particle dimensions. TEM images, reported in Figure 1, give also information about the morphology of Au NS samples: all shells are roughened and inhomogeneous. Au NS III is the sample with the least coverage degree, while Au NS II is the most covered one. Au NS I and III present a lower degree of coverage than Au NS II and IV, respectively.

The extinction spectra of nanoshells, reported in Figure 2, show that the LSPR band maximum position lies between 620 and 680 nm. The shell thickness influences the maximum wavelength position: for samples with the same core dimension, a red shift of the LSPR band is visible, moving from the smaller to the bigger final radius. Sample Au NS II is red shifted of about 20 nm with respect to Au NS I, and sample Au NS IV shows a red shift of 60 nm with respect to Au NS III. In Au NSs III and IV spectra a shoulder is slightly visible at around 550-600 nm, while it is less evident in Au NS I and seems to be absent in Au NS II.
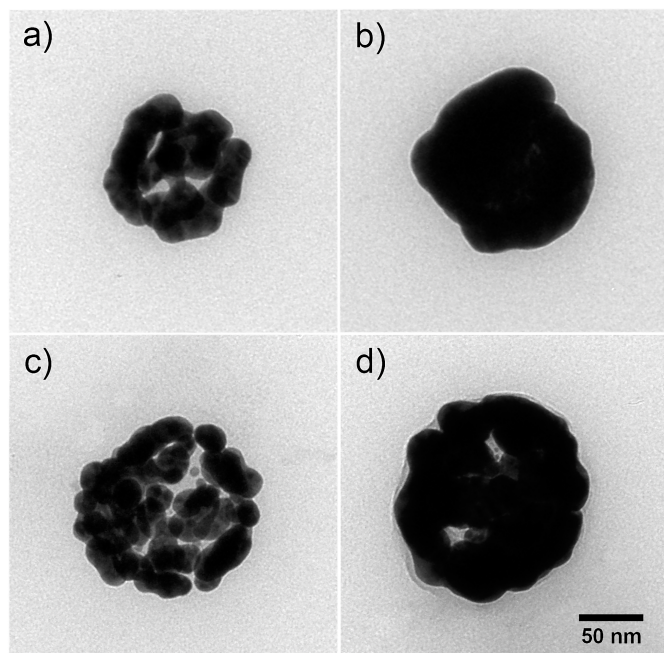
Fig. 1 TEM images of Au NSs samples: (a) Au NS I, (b) Au NS II, (c) Au NS III, (d) Au NS IV.

The LSPR maximum positions depend on the R1/R2 ratio[14] and the total R2 dimension.[18] As described by Oldenburg et al. in 1998, for ideal nanoshell systems, with perfectly covered and smooth shells, a red shift of the LSPR band is theoretically predicted at increasing R1/R2 ratio, that is for the same silica core at decreasing shell thicknesses. Moreover, Jain et al. in 2006,[18] described a red shift with increasing R2, at same R1/R2 ratio.
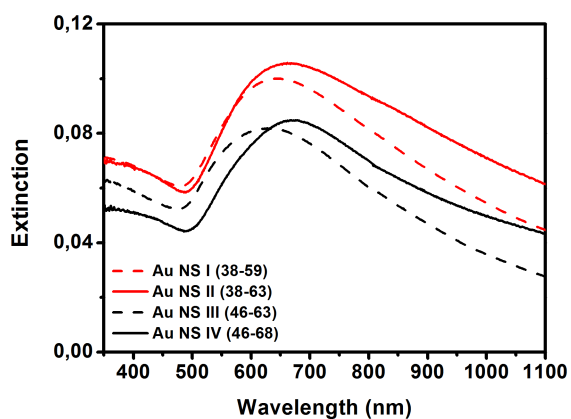

Fig. 2 Extinction spectra of nanoshell samples: Au NS I and II with core radius of 38 nm (red) and Au NS III and IV with core radius of 46 nm (black).

The results, reported in Figure 2, are not in agreement with this statement, but can be understood through the work by Preston and Signorell.[36] These authors studied the kinetics of the gold nanoshell formation, during precursor reduction. They demonstrated, through DDA calculations and experimental data on 229 nm diameter nanoparticles, that core-shell systems, with incomplete shell coverage, show a clear red shift at decreasing R1/R2 ratio.

Moreover these nanoparticles display an additional high energy band, at around 500-600 nm, which decreases at increasing gold amount. At perfectly smooth and complete shell this band disappears. In Au NSs I, III and IV spectra the shoulder, visible at around 550-600 nm, seems to be the high energy band, just described. Due to the higher coverage of Au NS II, the high energy band is not evident. The red shift entity seems to be correlated to the difference in the coverage degree between samples with same core.

3.2 Photoacoustic spectroscopy

The LSPR extinction bands are expected to be the sum of an absorption and a resonant scattering contribution, as this is a general feature of metal nanoparticles with a considerable size, following the relationship between absorption, scattering and extinction cross sections: $\sigma_E = \sigma_A + \sigma_S$.[37] We have experimentally determined the absorption profile within the LSPR extinction bands of Au NS I, Au NS II and Au NS IV by means of PAS. The reason for exploiting this method is that the PAS signal, being generated by a photothermal process involving absorption and heat release, is intrinsically insensitive to light scattering.[38] Therefore, scattering contributions will be the cause of an amplitude loss when the PAS signal of a nanoparticle sample is compared with that of a calorimetric reference. This is a substance which immediately releases all the energy absorbed from the excitation light as heat,[39] and negligibly scatters. Figure 3 displays a typical measurement of this kind, performed for Au NS I at 772 nm excitation wavelength.
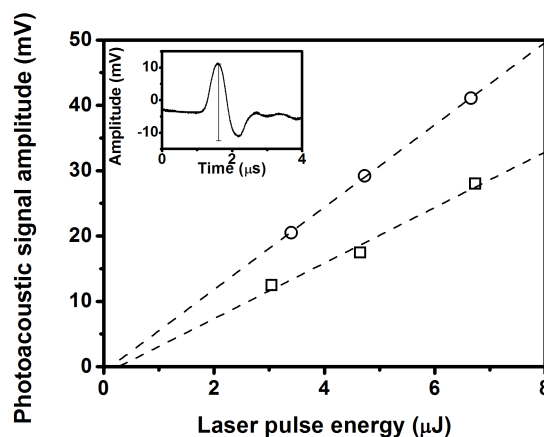

Fig. 3 A typical plot of the photoacoustic signal amplitude (indicated as the vertical bar in the inset, i.e., the difference between the first maximum and minimum) measured at increasing laser pulse energy for Au NS I (squares) and for the calorimetric reference $CuSO_4$ (circles), at 772 nm excitation wavelength.

The PAS signal amplitude (see inset) is recorded at increasing incident energy for both sample and reference, and the data is linearly fitted. The observed signal linearity rules out effects due to nonlinear processes[40] or nanoparticle reshaping.[41]
The signal of the Au NSs is proportional only to the absorption cross section. We assume that structural volume changes do not contribute to the PAS signal amplitude, as verified in the case of Au nanospheres.[30] Therefore, the ratio of the slopes of the fitting curves S_S/S_R (corrected for small extinction differences between sample, S, and reference, R) directly yields the ratio

between Au NS absorption and extinction cross sections, as the denominator in the following equation is unity:

$$\frac{S_S}{S_R} = \frac{(\sigma_A/\sigma_E)_S}{(\sigma_A/\sigma_E)_R}$$

The measurement is repeated at different excitation wavelengths for Au NS I, II and IV, resulting in the photoacoustic excitation profiles shown in Figure 4 (upper panels). The absorption spectral profiles, $\sigma_A(\lambda)$ (middle panels)

are then obtained from the product of the normalized extinction spectra with the σ_A/σ_E ratio. Finally, the difference $\sigma_E-\sigma_A$ yields the scattering spectral profiles $\sigma_S(\lambda)$ (lower panels). An apparent feature is that $\sigma_A(\lambda)$ and $\sigma_S(\lambda)$ do not coincide, the latter being red-shifted by approximately 100 nm for all Au NS samples. Moreover, the relative absorption contribution within the extinction band decreases in the order AuNS I > Au NS II > AuNS IV.
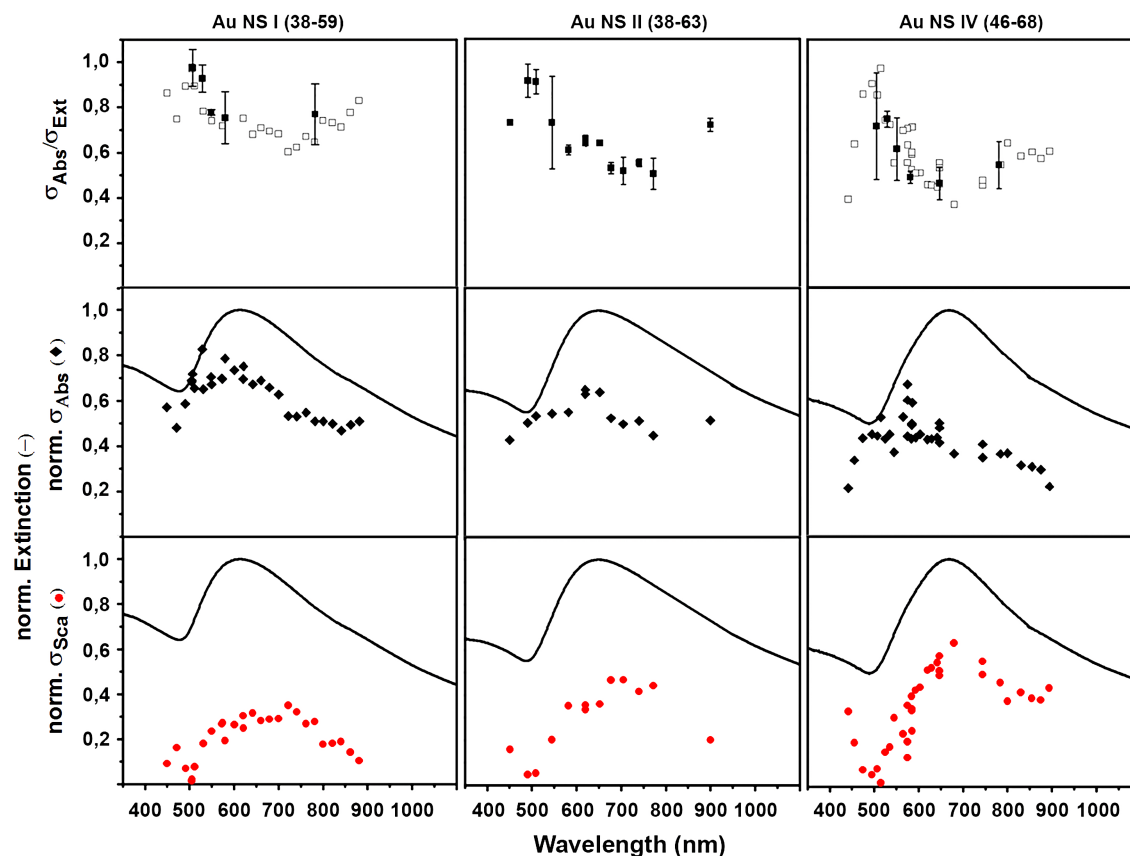

Fig. 4 *Upper panels*: ratio of the PAS signal amplitude for the sample and for the calorimetric reference (S_S/S_R), equivalent to the σ_A/σ_E ratio. The error bars are the standard deviation of the fitting curves of the kind shown in figure 3, considering the error propagation when taking the ratio of the fitting curve slopes. The points without error bars correspond to measurements at single laser energy. *Middle panels*: wavelength dependence of the normalized σ_A (obtained multiplying the normalized experimental extinction spectrum by the σ_A/σ_E ratio from the upper panels). *Lowest panels*: wavelength dependence of the normalized σ_S, obtained from the difference $\sigma_E-\sigma_A$.

3.3 Surface-enhanced Raman spectroscopy

The SERS EF profile measurements were carried out on Au NS solutions, using TBA as Raman probe. In Figure 5 the SERS spectrum of TBA on Au NSs II is reported ($\lambda_{exc} = 840$ nm), along with the Raman spectra of pure TBA and ethanol (EtOH) in water: all spectra were measured under the same experimental conditions. The pure TBA Raman spectrum was divided by a factor 100, to make it comparable to the others.
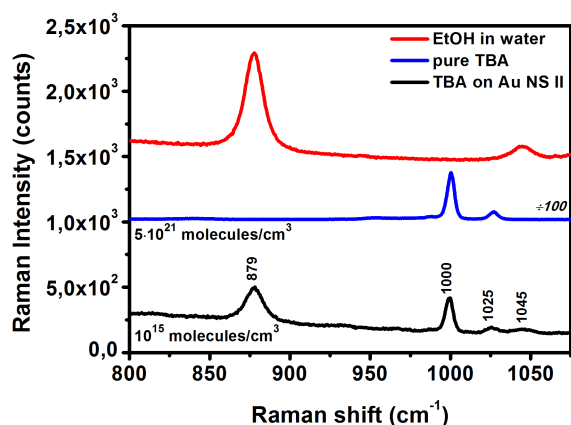
Fig. 5 SERS spectrum of TBA on Au NS II (black) and Raman spectra of pure TBA (blue) and ethanol in water (red), obtained with 840 nm excitation wavelength, under same experimental conditions. The spectra are vertically shifted for a better visualization.

The SERS signals of TBA and EtOH in the Au NS II solution are well visible. By comparing the TBA Raman mode intensity at about 1000 cm^{-1} in the NS solution with that of the pure TBA and considering the molecular concentrations in pure TBA and in TBA containing NS solution ($5 \cdot 10^{21}$ and 10^{15} molecules/cm^3 respectively), the EF turns out to be approximately $5 \cdot 10^4$ at 840 nm. In this calculation, it is assumed that all TBA is adsorbed on the Au NS surface. Moreover, the EtOH Raman signal at 879 cm^{-1} in the SERS sample is less intense than in water, although the EtOH concentration is the same. This is due to the effect of absorption of both the excitation and Raman-scattered light by the Au NS.

Table 2. Wavenumbers and assignments of the Raman bands in Figure 5.

Raman band position [cm^{-1}]	Assignment [34,42]
879	ν_{C-C} (ethanol)
1000	S_{12} (TBA)
1025	S_{18a} (TBA)
1045	ν_{C-O} (ethanol)

In Figure 6 the SERS EF profiles of Au NS solutions are reported. The SERS data are acquired at 568 and 647 nm and every 20 nm in the spectral range from 680 to 920 nm. For Au NS II sample, SERS data, acquired at 633 e 785 nm with the micro-Raman setup, are reported (black rhomboids). The reliability of the method used to carry out experimental absolute EF values is confirmed by the consistence of micro- and macro-Raman results; a direct comparison of data measured with these two setups has never been reported in literature before.
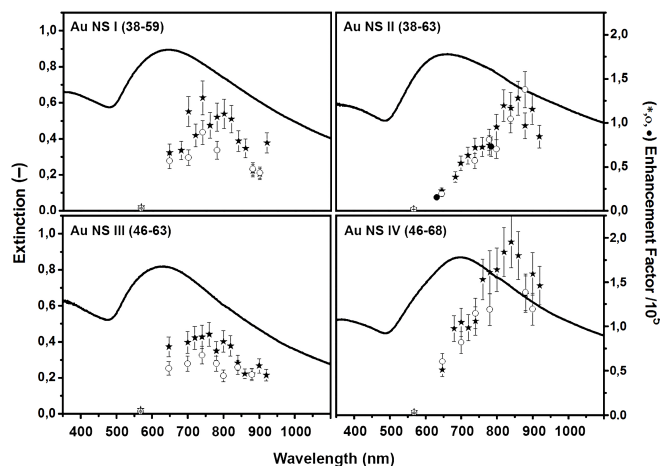

Fig. 6 Wavelength scanned EF measurements of Au NS I, II, III and IV, using TBA as Raman probe molecule: extinction spectra (black line) and EF profiles, first measurement run (black stars) and second one (white circles). Black dots for Au NS II sample are measured with the micro-Raman setup, to compare the EF values obtained with that of the tunable macro-Raman setup. The extinction spectra are arbitrarily scaled to allow a comparison with the spectral distribution of the Raman EF's.

The comparison between the first measurement run (full stars) and the second one (empty circles) shows that neither large changes in the EF values nor changes in the wavelength distribution occur for all samples within few days: this means that the data in Figure 6 have not been strongly influenced by short time aging or precipitation issues. This is different for long term stability: one month after functionalization, Au NS I and III did not show any TBA signal anymore, while Au NS II and IV showed a signal decrease of more or less one order of magnitude, but still visible and with the same EF spectral shape of the fresh sample. This difference in stability may be related to the Au coverage degree of NSs. The EF values of Au NS samples range between $4 \cdot 10^3$ and $2 \cdot 10^5$. For Au NS I and III, the highest EF values are observed between 700 and 800 nm. For thicker shells (Au NS II and IV), the EF band peaks at about 850 nm. Au NS IV shows the highest EF increase in going from $4 \cdot 10^3$ at 568 nm to $2 \cdot 10^5$ at 850 nm. As can be observed in all EF profiles, the SERS enhancement maxima are strongly red shifted with respect to those of the LSPR extinction bands, by about 150-200 nm. Finally, Au NS II and IV show sharper profiles than the other two samples.

4. Discussion

The combination of PAS and SERS has allowed us to determine the wavelength dependence of some relevant quantities for Au NSs with different core and shell dimensions: the absorption within the LSPR extinction band – a far-field property – and the SERS EF – a near-field property. The points of major interest in this study are: (i) the separation of the absorption and scattering components of the extinction spectra, (ii) the red shift of the scattering maximum with respect to the absorption maximum (iii) the red-shift of the SERS EF patterns with respect to both absorption and scattering profiles for all Au NSs.

Results (i) and (ii) are reasonably expected on the basis of Mie theory, which can be applied to spherical particles giving exact solutions for the wavelength dependence of the cross sections for the far-field related processes, absorption and scattering.[18] Both σ_A and σ_S are predicted to contribute to the extinction, σ_A

becoming less important as the particle radius becomes larger.[43] The relative σ_A decrease is true for both spherical nanoparticles and spherical nanoshells, when the total radius is considered. In fact, the results shown in Figure 4 clearly display this trend for Au NSs. In the case of Au nanospheres, a decrease of σ_A with growing diameter has been observed by the same photoacoustic method shown here.[30] Similarly, the absorption cross section of Au-Ag nanocages with two different sizes has been determined by PAS at the single wavelength of 638 nm, resulting lower for the larger nanocages.[44] Related results have been occasionally reported for other metal nanoparticle types, based on photothermal methods.[20,41,45,46] Alternatively, the direct measurement of the scattering cross section has been performed, allowing the determination of the same plasmonic properties.[21,22,47] As regards calculations, Mie theory can provide the wavelength dependence of the absorption and scattering contributions. The latter, compared to absorption, is shifted to longer wavelengths independently of NP shape, size, and composition, and our Au NSs follow this behaviour. Two features of Au NS IV, in particular, match favourably with those calculated in literature for silica/gold NS with R1 = 50 nm and R2 = 70 nm:[18] a difference of $\sim$ 30 nm between the extinction and scattering maximum wavelength (calculated: 26 nm), and a $\sim$ 0.6 σ_A/σ_E ratio (calculated: 0.69). A very good agreement between Mie theory predictions and observed resonant scattering has been reported for homogeneously covered single Au NSs, with R1 52÷60 nm and R2 72÷80 nm, where the scattering contribution was found to be predominant at long wavelengths.[17]

An interpretation on the basis of Mie theory is less straightforward for result (iii), that is, a strong red-shift of the SERS EF excitation profiles. In the hypothesis that the wavelength dependence of near-field properties is governed by the same metal resonances responsible for the spectral distribution of far-field properties, one should expect the SERS excitation profile to lie close to the extinction band.[12] This relation has been theoretically verified for small nanoparticles[48] and in an ordered array of nanotriangles.[49] Several factors can influence the relation between SERS EF profile and extinction to different extents.[50] For example, it has been recently theoretically shown that the damping of the surface plasmon resonance leads to a moderate red shift of the local field enhancement compared to the extinction band.[51] A second reason is intrinsically related to the SERS experiment. EF's depend on the wavelength of both excitation and Raman-scattered radiations, owing to the relationship between SERS enhancement and the product $|E(\lambda_{ex})|^2|E(\lambda_s)|^2$, where E is the electric field amplitude at the excitation and scattered wavelength. This dependence has been experimentally shown to give blue-shifted SERS excitation profiles.[49] However, the factor that most strongly affects the SERS EF profiles, often leading to a complete breakdown of any relation with extinction is the non-ideality of SERS substrates, which are often heterogeneous. The most frequently encountered case is that of small amounts of NP aggregates, resonant at longer wavelength with respect to isolated NPs, that do not significantly influence the extinction spectra, but that are very efficient in amplifying the Raman scattering, up to 3-4 orders of magnitude more than isolated nanoparticles.[52–54] In the previous sections we mentioned that PVP was added to the solution in order to avoid the formation of aggregates and DLS measurements did not show their presence: nevertheless, due to the extreme sensitivity of Raman to aggregates, we cannot rule out their contribution to the SERS EF profiles. In this regard, even when

a TEM analysis does not give evidence for the presence of clusters, their contribution can still be dominant in the solution.[55] Another source of heterogeneity originates from the presence of small defects, like gaps and tips, even on a single NP. They are mostly referred to as hot spots.[56] This aspect can be particularly relevant for thin-shell NSs, which are often irregularly coated. For example, roughened Au NSs provide increased amplifications of the local field of about 10^3 with respect to the smooth ones. Hot-spot resonances for Au-based materials lie in the near-infrared region,[57,58] where we observe a maximum in the SERS EF wavelength dependence.

Conclusions

SERS enhancement reaches a maximum in the red near-infrared region for Au NSs. We have demonstrated this effect for NSs with different core and shell sizes in an unusually extended wavelength range. Red shift of the EF profile with respect to the LSPR extinction band is observed in all of the examined cases. Moreover, as we could selectively assess the absorption and scattering contributions to extinction by PAS, we have verified that the EF profile is not only redshifted compared to extinction, but even compared to scattering. In fact, this behaviour can be expected on the basis of general considerations and experimental constraints. A general aspect of SERS is its being dominated by the local field enhancement occurring at the metal surface due to the plasmonic resonance. Therefore, the SERS enhancement, contrary to far-field absorption and scattering, also depends on the wavelength of the Raman-scattered radiation. In addition to this feature, which is valid for both ideal and real SERS-active metal substrates, the presence of hot spots in real samples can strongly affect the wavelength dependence, as the hot spot resonances are largely redshifted. This appears to be the case of the AuNSs we employed in this study. The different spectral distributions we have measured by SERS and PAS have practical consequences. Au NSs of the type we synthesized will be more suitable for dark-field imaging than for photothermal therapy, at least for wavelengths on the red side of the LSPR band. For SERS applications, near-infrared laser excitation will be more effective.

Notes and references

[a] Consorzio INSTM and Department of Chemical Science, University of Padova, Via Marzolo 1, 35131 Padova, Italy

[b] Department of Chemistry "Ugo Schiff", University of Firenze, Via della Lastruccia 3, 50019 Sesto Fiorentino (FI), Italy

1. C. Loo, L. Hirsch, M.-H. Lee, E. Chang, J. West, N. Halas, and R. Drezek, *Opt. Lett.*, 2005, **30**, 1012–4.

2.	X. Huang, P. K. Jain, I. H. El-Sayed, and M. a El-Sayed, *Lasers Med. Sci.*, 2008, **23**, 217–28.

3.	S. Lal, S. Link, and N. J. Halas, *Nat. Photonics*, 2007, **1**, 641–648.

4.	C. Loo, A. Lin, L. Hirsch, M.-H. Lee, J. Barton, N. Halas, J. West, and R. Drezek, *Technol. Cancer Res. Treat.*, 2004, **3**, 33–40.

5.	C. Loo, A. Lowery, N. Halas, J. West, and R. Drezek, *Nano Lett.*, 2005, **5**, 709–11.

6.	A. M. Gobin, M. H. Lee, N. J. Halas, W. D. James, R. a Drezek, and J. L. West, *Nano Lett.*, 2007, **7**, 1929–34.

7.	M. Hu, J. Chen, Z.-Y. Li, L. Au, G. V Hartland, X. Li, M. Marquez, and Y. Xia, *Chem. Soc. Rev.*, 2006, **35**, 1084–94.

8.	K. a Willets and R. P. Van Duyne, *Annu. Rev. Phys. Chem.*, 2007, **58**, 267–97.

9.	M. Fan, G. F. S. Andrade, and A. G. Brolo, *Anal. Chim. Acta*, 2011, **693**, 7–25.

10.	E. Fort and S. Grésillon, *J. Phys. D. Appl. Phys.*, 2008, **41**, 013001.

11.	S. A. Maier, *Plasmonics: Fundamentals and applications*, Springer, 2007.

12.	E. Le Ru and P. Etchegoin, *Principles of Surface-Enhanced Raman Spectroscopy: and related plasmonic effects*, Elsevier, 2008.

13.	E. Prodan, C. Radloff, N. J. Halas, and P. Nordlander, *Science*, 2003, **302**, 419–22.

14.	S. J. Oldenburg, R. D. Averitt, S. L. Westcott, and N. J. Halas, *Chem. Phys. Lett.*, 1998, **288**, 243–247.

15.	S. Kalele, S. W. Gosavi, J. Urban, and S. K. Kulkarni, *Curr. Sci.*, 2006, **91**, 1038–1052.

16.	S. J. Oldenburg, G. D. Hale, J. B. Jackson, and N. J. Halas, *Appl. Phys. Lett.*, 1999, **75**, 1063.

17.	C. L. Nehl, N. K. Grady, G. P. Goodrich, F. Tam, N. J. Halas, and J. H. Hafner, *Nano Lett.*, 2004, **4**, 2355–2359.

18.	P. K. Jain, K. S. Lee, I. H. El-Sayed, and M. a El-Sayed, *J. Phys. Chem. B*, 2006, **110**, 7238–48.

19.	S. Lal, N. K. Grady, G. P. Goodrich, and N. J. Halas, *Nano Lett.*, 2006, **6**, 2338–43.

20.	U. Kreibig, B. Schmitz, and H. D. Breuer, *Phys. Rev. B*, 1987, **36**, 5027–5032.

21.	D. D. Evanoff and G. Chumanov, *J. Phys. Chem. B*, 2004, **108**, 13957–13962.

22.	W. Ni, X. Kou, Z. Yang, and J. Wang, *ACS Nano*, 2008, **2**, 677–86.

23.	P. L. Stiles, J. a Dieringer, N. C. Shah, and R. P. Van Duyne, *Annu. Rev. Anal. Chem. (Palo Alto. Calif)*, 2008, **1**, 601–26.

24.	G. a Baker and D. S. Moore, *Anal. Bioanal. Chem.*, 2005, **382**, 1751–70.

25.	S. Nie, *Science (80-.).*, 1997, **275**, 1102–1106.

26.	V. Joseph, A. Matschulat, J. Polte, S. Rolf, F. Emmerling, and J. Kneipp, *J. Raman Spectrosc.*, 2011, **42**, 1736–1742.

27.	J. B. Jackson and N. J. Halas, *Proc. Natl. Acad. Sci. U. S. A.*, 2004, **101**, 17930–5.

28.	G. Giallongo, G. A. Rizzi, V. Weber, G. Ennas, R. Signorini, and G. Granozzi, *Nanotechnology*, 2013, **24**, 345501.

29.	E. C. Le Ru, M. Dalley, and P. G. Etchegoin, *Curr. Appl. Phys.*, 2006, **6**, 411–414.

30.	A. Feis, C. Gellini, P. R. Salvi, and M. Becucci, *Photoacoustics*, 2014, **2**, 47–53.

31.	T. Pham, J. B. Jackson, N. J. Halas, and T. R. Lee, *Langmuir*, 2002, **18**, 4915–4920.

32.	W. Stöber, A. Fink, and E. Bohn, *J. Colloid Interface Sci.*, 1968, **26**, 62–69.

33.	D. G. Duff, A. Baiker, and P. P. Edwards, *Langmuir*, 1993, **9**, 2301–2309.

34.	G. Varsanyi, *Vibrational Spectra of Benzene Derivatives*, Akademiai Kiado-Budapest, 1969.

35.	E. C. Le Ru, E. Blackie, M. Meyer, and P. G. Etchegoin, *J. Phys. Chem. C*, 2007, **111**, 13794–13803.

36.	T. C. Preston and R. Signorell, *ACS Nano*, 2009, **3**, 3696–706.

37.	C. F. Bohren and D. R. Huffman, *Absorption and Scattering of Light by Small Particles*, Wiley, 2008.

38.	J. R. Small, N. S. Foster, J. E. Amonette, and T. Autrey, *Appl. Spectrosc.*, 2000, **54**, 1142–1150.

39.	S. E. Braslavsky and G. E. Heibel, *Chem. Rev.*, 1992, **92**, 1381–1410.

40.	C. S. Yelleswarapu and S.-R. Kothapalli, *Opt. Express*, 2010, **18**, 9020–5.

41.	V. Amendola and M. Meneghetti, *J. Mater. Chem.*, 2007, **17**, 4705.

42.	G. Socrates, *Infrared & Raman characteristic group frequencies : tables & charts*, Wilthshire, 1994.

43.	B. M. Ross and L. P. Lee, *Opt. Lett.*, 2009, **34**, 896.

44.	E. C. Cho, C. Kim, F. Zhou, C. M. Cobley, K. H. Song, J. Chen, Z.-Y. Li, L. V Wang, and Y. Xia, *J. Phys. Chem. C*, 2009, **113**, 9023–9028.

45. M. a van Dijk, a L. Tchebotareva, M. Orrit, M. Lippitz, S. Berciaud, D. Lasne, L. Cognet, and B. Lounis, *Phys. Chem. Chem. Phys.*, 2006, **8**, 3486–95.

46. V. Dijk, M. Lippitz, and M. Orrit, *Acc. Chem. Res.*, 2005, **38**, 594–601.

47. N. Micali, F. Mallamace, M. Castriciano, A. Romeo, and L. Monsú Scolaro, *Anal. Chem.*, 2001, **73**, 4958–4963.

48. J. B. Messinger, U. von Raben, R. K. Chang, and P. W. Barber, *Phys. Rev. B*, 1981, **24**, 649–657.

49. A. D. McFarland, M. a Young, J. a Dieringer, and R. P. Van Duyne, *J. Phys. Chem. B*, 2005, **109**, 11279–85.

50. E. C. Le Ru, C. Galloway, and P. G. Etchegoin, *Phys. Chem. Chem. Phys.*, 2006, **8**, 3083–3087.

51. J. Zuloaga and P. Nordlander, *Nano Lett.*, 2011, **11**, 1280–3.

52. M. D. Doherty, A. Murphy, J. McPhillips, R. J. Pollard, and P. Dawson, *J. Phys. Chem. C*, 2010, **114**, 19913–19919.

53. J. P. Litz, J. P. Camden, and D. J. Masiello, *J. Phys. Chem. Lett.*, 2011, **2**, 1695–1700.

54. S. L. Kleinman, B. Sharma, M. G. Blaber, A.-I. Henry, N. Valley, R. G. Freeman, M. J. Natan, G. C. Schatz, and R. P. Van Duyne, *J. Am. Chem. Soc.*, 2013, **135**, 301–308.

55. M. Moskovits, *Phys. Chem. Chem. Phys.*, 2013, **15**, 5301–11.

56. C. E. Talley, J. B. Jackson, C. Oubre, N. K. Grady, C. W. Hollars, S. M. Lane, T. R. Huser, P. Nordlander, and N. J. Halas, *Nano Lett.*, 2005, **5**, 1569–74.

57. L. Rodríguez-Lorenzo, R. A. Álvarez-Puebla, F. J. G. de Abajo, and L. M. Liz-Marzán, *J. Phys. Chem. C*, 2010, **114**, 7336–7340.

58. W. Xie, B. Walkenfort, and S. Schlücker, *J. Am. Chem. Soc.*, 2013, **135**, 1657–1660.

Physical Chemistry Chemical Physics Accepted Manuscript